RSC Advances

PAPER

View Article Online
View Journal | View Issue

Cite this: *RSC Adv.*, 2020, **10**, 21259

Correlating the size and cation inversion factor in context of magnetic and optical behavior of $CoFe_2O_4$ nanoparticles†

Jitendra Pal Singh, *[a] Jae Yeon Park, [b] Varsha Singh, [c] So Hee Kim, [c] Weon Cheol Lim, [c] Hemaunt Kumar, [d] Y. H. Kim, [a] Sangsul Lee *[ae] and Keun Hwa Chae *[c]

Herein, the size dependent behavior of cobalt ferrite nanoparticles was investigated using synchrotron radiation based techniques. Scanning electron micrographs revealed the enhancement of particle/crystallite size with increase of annealing temperature. Moreover, the shape of these particles also changed with increase of crystallite size. Saturation magnetization increased with increase of crystallite size. The higher saturation magnetization for larger crystallite size nanoparticles was attributed to a cation distribution similar to that of bulk $CoFe_2O_4$. The optical band-gap of these nanoparticles decreased from 1.9 eV to 1.7 eV with increase of crystallite size. The enhancement of the optical band-gap for smaller crystallites was due to phenomena of optical confinement occurring in the nanoparticles. Fe L Co L-edge near edge extended X-ray absorption fine structure (NEXAFS) measurements showed that Fe and Co ions remain in the 3+ and 2+ state in these nanoparticles. The results obtained from Fe & Co K-edge X-ray absorption near edge structure (XANES)-imaging experiments further revealed that this oxidation state was possessed by even the crystallites. Extended X-ray absorption fine structure (EXAFS) measurements revealed distribution of Fe and Co ions among tetrahedral (A) and octahedral (B) sites of the spinel structure which corroborates the results obtained from Rietveld refinement of X-ray diffraction patterns (XRD). X-ray magnetic circular di-chroism (XMCD) measurements revealed negative exchange interaction among the ions situated in tetrahedral (A) and octahedral (B) sites. Theoretical and experimental calculated magnetic moments revealed the dominancy of size effects rather than the cation redistribution in the spinel lattice of $CoFe_2O_4$ nanoparticles.

Received 21st February 2020
Accepted 26th May 2020

DOI: 10.1039/d0ra01653e

rsc.li/rsc-advances

Introduction

The underlying processes involved in the physical and chemical properties of nanoparticles are investigated *via* depicting the local electronic/atomic and magnetic structure using numerous techniques like electron energy-loss spectroscopy (EELS)[1,2] and neutron diffraction.[3] In addition to this, techniques based on synchrotron radiation show it's prominence over these techniques.[4] X-ray absorption spectroscopy (XAS),[5] X-ray magnetic circular dichroism (XMCD)[6] and X-ray absorption near edge structure (XANES)-imaging[7] are the well-known and effective tools based on this radiation. XAS is very much effective to determine local electronic/atomic structure in the nanoparticles whereas XMCD is able to provoke about the magnetic interaction in these nanoparticles.[5,6] The XANES-imaging technique determines local electronic structure of the materials with spatial resolution additive.[7] Thus, these techniques are able to give complete account of the local structure of the nanoparticle under investigation.[5–7] Since, size dependence of nanoparticle is common phenomena and bulk characteristics of these nanoparticles are investigated using numerous techniques, however, the appropriate reason roots at the atomic/molecular level.[8,9] Thus, a systematic and rigorous investigation using advanced techniques is needed at this level.

The nanoparticles of $CoFe_2O_4$ show immense opportunities for utilization in various fields of technological importance.[10,11] The nanoparticles of this material show potential for permanent magnet[12] spintronics,[13] photocatalysis,[14] battery industry,[15,16] biomedical applications[17] and many more depending upon it's magnetic,[12,13,17] optical[10,11,14] and structural behavior.[15,16] These various behaviors are controlled by the size, size distribution and occupancies of metal ions in the unit

[a]*Pohang Accelerator Lab, Pohang University of Science and Technology, Pohang 37673, Republic of Korea. E-mail: jitendra2029@postech.ac.kr; sangsul@postech.ac.kr*

[b]*Radiation Equipment Research Division, Korea Atomic Energy Research Institute, Jeongup 56212, Republic of Korea*

[c]*Advanced Analysis Center, Korea Institute of Science and Technology, Seoul 02792, Republic of Korea. E-mail: khchae@kist.re.kr*

[d]*Department of Applied Sciences, Rajkiya Engineering College, Bijnor-246725, India*

[e]*Xavisoptics Ltd., Pohang 37673, Republic of Korea*

† Electronic supplementary information (ESI) available. See DOI: 10.1039/d0ra01653e

cell.[10–17] The unit cell of this material in the bulk form represents the face centered cubic (fcc) structure configured by O^{2-} ions by forming tetrahedral (A) and octahedral (B)-sites to be filled by metal (Co^{2+} and Fe^{3+}) ions. Due to strong tendency of favoring octahedral coordination, whole Co^{2+} ions occupy B-site, however, Fe^{3+} ions distribute among A- and B-sites in equal proportion.[18] This makes this material inverse spinel, however, pre and post-synthesis treatment leads to distribution of these ions among A- and B-sites[10–17] as follows

$$(Co_{\lambda}Fe_{1-\lambda})_A[Co_{1-\lambda}Fe_{1+\lambda}]_BO_4 \quad (1)$$

where, λ represents fraction of Co ions migrated to A-site. Thus, distribution of metal ions play an important to control magnetic behavior that provide an opportunity to optimize this material for particular applications.[19–21] Additionally, optical behavior of this material is no less important,[14,22,23] however, it's size dependence and correlation with metal ion distribution remains obscure.

Numerous studies are available determining the metal ion distribution using Mössbauer spectroscopy[24] and neutron diffraction,[25] however, this investigation lacks using XAS even showing superiority over these techniques.[26] This technique is very much effective to determine metal ion distribution in nanoparticles[27,28] and thin film.[29] Hence, synchrotron radiation based techniques like XAS, XMCD and XANES-imaging are carried out to get deeper insights of size dependence of this material by investigating local electronic/atomic and magnetic structure.

Experimental

Synthesis procedure

Solutions of cobalt nitrate hexahydrate and ferric nitrate nonahydrate in stoichiometric proportion were mixed into citric acid solution by keeping the cations to citric acid ratio 1 : 2.[28] The mixture was kept on magnetic stirrer at 85 °C to get viscous solution for 2 h. The viscous solution was dried for almost 12 h by heating between 100 °C on a hot plate to form precursor. Precursor thus obtained was further annealed at 300, 500, 700 and 900 °C to synthesize nanoparticles of different size.

Characterization

X-ray diffraction (XRD) patterns of synthesized nanoparticles were recorded at D/MAX2500 (RIGAKU, Japan) X-ray diffractometer using Cu Kα ($\lambda = 1.5418$ Å) radiation. Scanning electron microscopic (SEM) measurements were carried out using Hitachi (S-4200) field emission scanning electron microscope (FE-SEM). Magnetic measurements at room temperature were performed on vibrating sample magnetometer (VSM). Optical behavior of these nanoparticles was investigated using Carry 5000 UV-Vis spectrometer.

Synchrotron radiation based characterization

Various synchrotron radiation based experiments were performed at Pohang Accelerator Laboratory (PAL), Pohang, South Korea. This laboratory is able to operate at 3.0 GeV energy with a maximum storage current of 360 mA.[30]

Near edge X-ray absorption fine structure (NEXAFS) measurements for these nanoparticles were performed at 10D XAS KIST (Korea Institute of Science and Technology) beamline. NEXAFS spectra of these nanoparticles were collected in the total electron yield (TEY) mode and were normalized with respect to post-edge height after background subtraction. Extended X-ray absorption structure (EXAFS) spectra were measured at 1D KIST beamline while detuning incident beam to 50% of maximum intensity, which enable removal of higher harmonics. The detailed experimental procedure is depicted elsewhere.[27–29]

Room temperature XMCD experiments at $L_{2,3}$ edges of Fe were performed at 2A beamline which utilizes circularly polarized light with a degree of circular polarization around 80% and an electromagnet of magnetic field strength μ_0H (between -0.75 and 0.75 T) for measurements.[31] The absorption data were collected in the TEY mode by applying voltage of 200 V. The photon beam and the magnetic field were perpendicular to the sample plane. The base pressure of the system was 10^{-9} Torr. The absorption was normalized to the incoming photon beam intensity by measuring simultaneously the photocurrent at Au grid.

XANES-imaging measurements were carried out at 7C beamline, which utilizes off-axis illumination of X-ray to capture image using a charge-coupled device (CCD). Zone plate with 150 μm diameter and 40 nm outermost width was used to get transmission X-ray images. This arrangement is able to give spatial resolution of 40 nm and field of view of around 35 μm.[32,33]

For these measurements, X-ray energy was varied from -20 to 80 eV from the main edge energy of Fe and Co K-edge with an interval of 1 eV. The actual values of energy variation are shown in Table S1.†

Simulation details

XRD patterns of these nanoparticles were refined using FullProf program based on Rietveld analysis.[22] The space group $Fd\bar{3}m$ was assumed, with the 8a, l6d cation sites and 32e O sites all fully occupied.[14] Values of goodness of factor (GOF) obtained for these refined patterns vary from 1.1 to 1.5.

The program Athena was used to sum the data, identify the beginning of the absorption edge (E_0), fit pre- and post-edge backgrounds, and hence to obtain the normalized absorbance, χ, as a function of the modulus of the photoelectron wave vector, k.[34] The EXAFS data is Fourier transformed to R-space to investigate the atomic structure and relative bond-lengths with respective to absorbing atoms.[35] The fitting was carried out using ARTEMIS in the k range 3–11.5 $Å^{-1}$ (Co) and 3–9 $Å^{-1}$ (Fe). The theoretical structure for $CoFe_2O_4$ was generated using the ATOM and FEFF from the parameters obtained from Rietveld refinement.[34,35]

The transmission images were processed with background correction and image registration to extract XANES spectrum at single pixel using the lab-made software based on LabVIEW program.[36] From these images, XANES spectra are extracted for single-pixel and for the whole image.

Results

Crystalline phase, size and strain analysis

Fig. 1 shows fitted XRD patterns of synthesized nanoparticles at annealing temperature of 300, 500, 700 and 900 °C. It is clear from Fig. 1 that both the experimental and simulated data points are in close correlation with each other. This indicates that all the peaks in XRD pattern are associated with *Fd3m* space group of spinel structure. Thus, synthesized nanoparticles exhibit presence of cubic spinel phase [JCPDS no. # 01-1121]. No other peak corresponding to any impurity phase is being detected in these patterns. Refined and simulated parameters from Rietveld refinement are collated in Table 1.

The values of lattice parameter are 8.357 ± 0.005, 8.382 ± 0.002, 8.384 ± 0.002 and 8.386 ± 0.007 Å for annealing temperature of 300, 500, 700 and 900 °C respectively. Thus, lattice parameter approaches towards the value of bulk $CoFe_2O_4$ with increase of annealing.[37]

Another, important observation from this refinement is the distribution of cations (Co^{2+} and Fe^{3+} ions) among A- and B-sites. The value of Fe^{3+} ion occupancy is 0.556 ± 0.003, 0.624 ± 0.003, 0.649 ± 0.004 and 0.706 ± 0.004 at B-site for annealing temperature of 300, 500, 700 and 900 °C. Thus, this value is approaching towards 1, which is the behavior of bulk $CoFe_2O_4$ and concurrent with the variation of lattice parameter with annealing as discussed earlier. This means higher annealing help to achieve the perfect inverse spinel structure for $CoFe_2O_4$.

Crystallite size (D) of these nanoparticles were estimated from most intense (311) peak using Scherrer's formula,[26]

$$D = 0.94\lambda/\beta \cos\theta \quad (2)$$

where, symbols have their usual meanings. Values of crystallite size estimated for different annealing temperatures are collated in Table 1. The values of crystallite size are 9 ± 1, 22 ± 2, 49 ± 4 and 61 ± 6 nm for annealing temperature of 300, 500, 700 and 900 °C respectively.

Thus, values of lattice parameters, cation occupancies and crystallite size envisage that higher annealing results in the bulk like characteristics of nanoparticles. This kind of behavior is also observed for other ferrite systems as well.

The X-ray density (ρ_x) of these nanoparticles is determined from following relation

$$\rho_x = \frac{ZM}{NV} \quad (3)$$

where, Z is number of nearest neighbor, M is molecular weight, N is Avogadro number and V is volume of unit cell ($V = a^3$). Estimated values of X-ray densities are 5.31 ± 0.02, 5.46 ± 0.02, 5.61 ± 0.02 and 5.73 ± 0.02 g cm^{-3} for 300, 500, 700 and 900 °C respectively (Table 1). Thus, annealing improves the density of synthesized nanoparticles.

In most of the nanoparticle, strain also exhibits variation with change of nanoparticle size or processing parameters, hence, the strain is estimated by using Williamson–Hall (W–H) plot methods.[38] The W–H plots based on the equation given below are shown in Fig. 1.

$$\beta \cos\theta = \frac{0.94\lambda}{D_{WH}} + 4\varepsilon_i \sin\theta \quad (4)$$

where, D_{WH} is size estimated from this method. The values of various parameters are shown in Table 1. The variation of crystallite size with annealing temperature estimated from this method is analogues to that obtained from Scherrer's formula.

The estimated strain has negative value for the nanoparticles annealed at 300 and 500 °C. Negative value of strain is observed for numerous ferrite nanoparticle systems and associated with presence of compressive strain.[39,40] Strain has positive value for the annealing temperature of 700 and 900 °C in agreement with previous studies on cobalt ferrite nanoparticles of similar size.[41]

Size and morphology

Fig. 2 shows the SEM micrographs of nanoparticles synthesized at 300, 500, 700 and 900 °C. SEM micrographs of nanoparticles synthesized at 300 and 500 °C exhibit bunch of several small particles. These nanoparticles contains particles with almost spherical shape. SEM micrograph of $CoFe_2O_4$ nanoparticles synthesized at 700 °C contains mixture of particles with hexagonal type shape and deviated spherical shape (Fig. 2).

When these nanoparticles are obtained at 900 °C, most of them attain hexagonal type shape. Almost spherical shape of nanoparticles is observed for ferrite nanoparticles and are reported by number of authors.[42,43] These authors also observe formation of hexagonal type particle shape at higher sintering temperature. A schematic of shape modification is presented in Fig. 3a.

The information on particle size is obtained from these measurements. The size of almost 150 particles were measured using ImageJ software and size distribution curves of these nanoparticles are shown in Fig. 3b. The particle size estimated from these size distribution curves are 19 ± 9, 32 ± 17, 124 ± 101 and 242 ± 142 nm for annealing temperature of 300, 500, 700 and 900 °C respectively.[44,45] Thus, variation of particle size with annealing temperature is concurrent with the crystallite size obtained from XRD pattern.

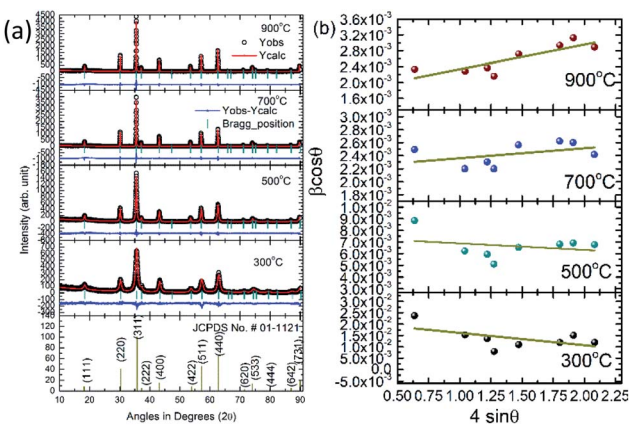

Fig. 1 (a) XRD patterns along with JCPDS-01-1121 and (b) W–H plots of $CoFe_2O_4$ nanoparticles synthesized at 300, 500, 700 and 900 °C.

Table 1 Simulated parameters estimated from Rietveld refinement of X-ray patterns

			$CoFe_2O_4$ nanoparticles			
Parameters			300 °C	500 °C	700 °C	900 °C
Lattice parameter; a (Å)			8.357 ± 0.005	8.382 ± 0.002	8.384 ± 0.008	8.386 ± 0.007
Oxygen positional parameter; u (Å)			0.2558 ± 0.0004	0.2562 ± 0.0003	0.2556 ± 0.0004	0.2551 ± 0.004
Occupancy	A-site	Co^{2+}	0.446 ± 0.003	0.376 ± 0.003	0.351 ± 0.004	0.294 ± 0.004
		Fe^{3+}	0.556 ± 0.003	0.624 ± 0.003	0.649 ± 0.004	0.706 ± 0.004
	B-site	Co^{2+}	0.556 ± 0.003	0.624 ± 0.003	0.649 ± 0.004	0.706 ± 0.004
		Fe^{3+}	1.446 ± 0.003	1.376 ± 0.003	1.351 ± 0.004	1.294 ± 0.004
Bragg R-factor			7.99	6.48	5.75	5.57
Rf-factor			5.52	3.43	3.47	3.10
Goodness of fit (GOF)-index			1.1	1.1	1.5	1.4
Crystallite size; D (nm)			9 ± 1	22 ± 2	49 ± 4	61 ± 6
X-ray density; ρ (g cm^3)			5.31 ± 0.02	5.46 ± 0.02	5.61 ± 0.02	5.73 ± 0.02
Crystallite size; D_{WH} (nm)			7 ± 1	19 ± 3	66 ± 6	84 ± 12
Strain ($\times 10^{-4}$), ε_i			−54 ± 32	5.6 ± 8.7	1.5 ± 1.3	6.2 ± 1.7

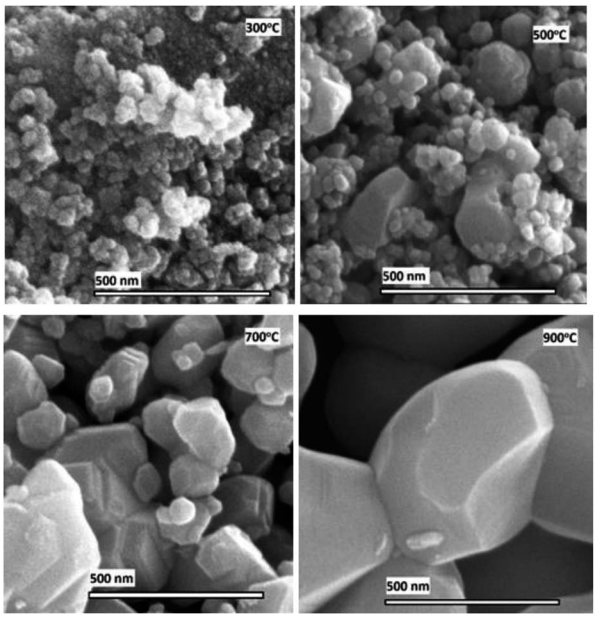

Fig. 2 Scanning electron micrographs of $CoFe_2O_4$ nanoparticles having annealing temperature of 300, 500, 700 and 900 °C.

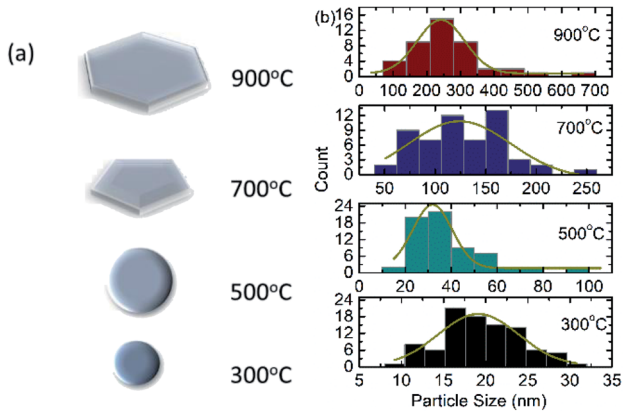

Fig. 3 (a) Particle shape overview and (b) size distribution estimated from SEM for $CoFe_2O_4$ nanoparticles annealed at 300, 500, 700 and 900 °C.

Magnetic behaviour

Fig. 4 shows the hysteresis curves of $CoFe_2O_4$ nanoparticles synthesized at 300, 500, 700 and 900 °C. These hysteresis curves show remanence and coercive behavior, which modifies with crystallite size.

Thus, these curves exhibit ferrimagnetic kind behavior of synthesized nanoparticles. This behavior is general characteristics of ferrites nanoparticles and is observed by number of researchers.[21,22,28,46]

The saturation magnetization of these nanoparticles are 52 ± 2, 66 ± 2, 70 ± 2 and 81 ± 2 emu g^{-1} for annealing temperature of 300, 500, 700 and 900 °C (Fig. 5a). The value of saturation magnetization at 900 °C is close to the value of bulk $CoFe_2O_4$.[37,42,43]

Thus saturation magnetization (σ_s) increases with increase of crystallite size according to the following linear relation.

$$\sigma_s = (0.5 \pm 0.1) \times D + (49 \pm 4) \quad (5)$$

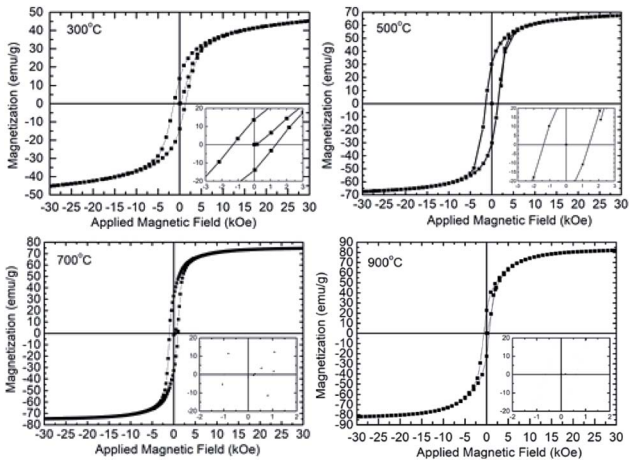

Fig. 4 Hysteresis curves of $CoFe_2O_4$ nanoparticles synthesized at 300, 500, 700 and 900 °C.

The magnetic moment per formula unit for these nanoparticles is calculated from saturation magnetization (σ_s) and molecular weight (M) of the material using the relation given below[28]

$$\mu_B = \frac{\sigma_s \times M}{5585} \quad (6)$$

Behavior of magnetic moment with crystallite size is analogues to that of saturation magnetization (Fig. 5b).

The remnant magnetization (σ_r) of these nanoparticles is represented by exponential decay function as follow (Fig. 5c)

$$\sigma_r = (1.3 \pm 0.1) + (-1.2 \times 10^{-25} \pm 1.2 \times 10^{-20}) \times e^{-(0.9\pm0.2)\times D} \quad (7)$$

The behavior of coercivity (H_c) with crystallite size (D) is represented by a parabolic function (Fig. 5d).

$$H_c = (2.3 \pm 0.2) \times D - (0.030 \pm 0.002) \times D^2 - (5.5 \pm 1.5) \quad (8)$$

A detailed investigation carried out by Li *et al.* (2017) for Fe_3O_4 nanoparticles envisages decrease of both remanent magnetization and coercivity with increase of size even the saturation magnetization increases. This behavior was explained because of exceeding single domain size limit above certain particle size.[47]

Optical behaviour

UV-Vis spectra of cobalt ferrite nanoparticles in diffuse reflectance mode are shown in Fig. 6a. The optical band-gap of these nanoparticles are determined from following relation

$$E_g = \frac{1237.5}{\lambda} \text{eV} \quad (9)$$

where, λ is wavelength corresponding to intercept on wavelength axis as shown in Fig. S1.† This kind of simple approach was used by Llanes *et al.* for estimation of optical band-gap in oxide nanoparticles.[48]

The optical-band gaps of these nanoparticles are 1.90 ± 0.02, 1.85 ± 0.02, 1.80 ± 0.02 and 1.69 ± 0.02 eV for nanoparticles annealed at 300, 500, 700 and 900 °C. Thus, optical band-gap decreases with increase of crystallite size and enhances with decrease of crystallite size (Fig. 6b). Similar enhancement of optical band-gap with decrease of crystallite size for zinc ferrite nanoparticle is also observed.[49] The enhancement of optical band-gap for small sized nanoparticle is explained using quantum confinement.[49,50] According to quantum confinement the optical band-gap of nanoparticle is written as

$$E_g = E_{bulk} + \frac{h^2}{8R^2}\left(\frac{1}{m_h^*} - \frac{1}{m_e^*}\right) - 0.248E_{Ry}^* \quad (10)$$

where, E_{bulk} is the optical band-gap of the bulk and E_{Ry}^* is the bulk excitation energy, h is Planck's constant, R is radius of nanocrystals. This clearly shows increase of optical band gap with decrease of crystallite size.

Synchrotron radiation based investigation

Local electronic structure

Oxidation state of metal ions. Fig. 7a shows Fe L-edge spectra of cobalt ferrite nanoparticles synthesized at 300, 500, 700 and 900 °C. Spectral features in the spectra of these nanoparticles are represented by A_1, A_2, and A_3 centered at 708.3 ± 0.1, 719.9 ± 0.1 and 721.5 ± 0.1 eV, respectively. In addition to this, shoulders S_1 and S_2 centered at 706.5 ± 0.1 and 711.7 ± 0.1 eV also exist in the spectra of these nanoparticles. These spectral features are associated with presence of Fe^{3+} ions in tetrahedral and octahedral crystal field.[26,27,51,52] Further, Fe K-edge spectra reflect spectral features A_1', A_2', A_3', A_4' and A_5' centered at 7132.1 ± 0.4, 7139.3 ± 0.4, 7146.7 ± 0.4, 7155.7 ± 0.4 and 7184.4 ± 0.4 for all nanoparticles synthesized at various annealing temperatures. In addition, a pre-edge spectral feature A_o', centered at 7114.1 ± 0.4 eV is observed in the spectra of these nanoparticles. Presence of pre-edge in the Fe K-edge spectra of ferrites is common. The intensity of pre-edge spectral features modifies with annealing temperature (Fig. 7b: inset).

The main edge for these nanoparticles occurs at 7121.7 ± 0.4, 7121.1 ± 0.4, 7121.0 ± 0.4 and 7120.1 ± 0.4 eV for annealing temperature of 300, 500, 700 and 900 °C. Thus, main edge slightly shifts to lower value with increase of annealing temperature (Fig. 7b). The main energy exhibits a shift of around 1.6 ± 0.8 eV when annealing temperature increases to

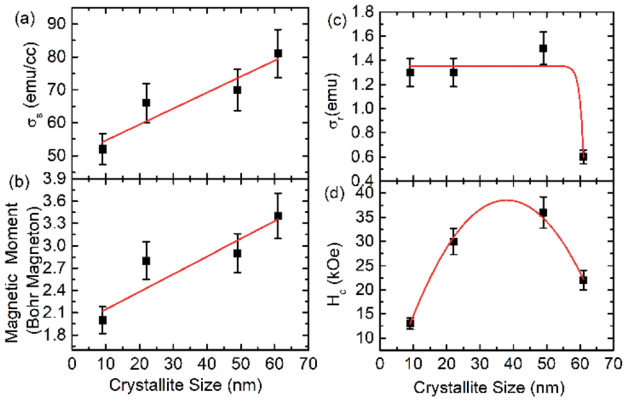

Fig. 5 (a) Saturation magnetization, (b) magnetic moment (c) remanent magnetization and (d) coercivity as a function of crystallite size.

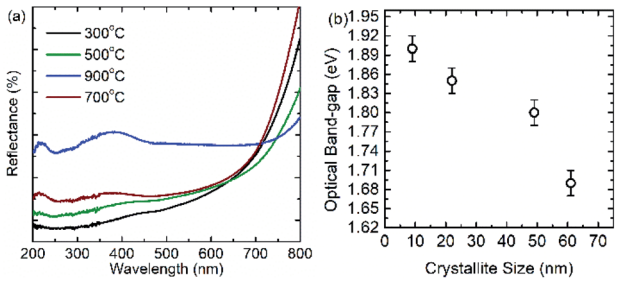

Fig. 6 (a) Optical behavior of $CoFe_2O_4$ nanoparticles synthesized at 300, 500, 700 and 900 °C. (b) Optical band-gap of nanoparticles as a function of crystallite size.

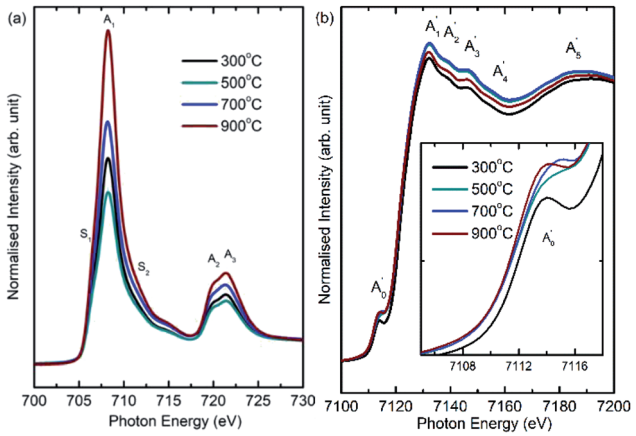

Fig. 7 (a) Fe L-edge and (b) Fe K-edge spectra of $CoFe_2O_4$ nanoparticles synthesized at 300, 500, 700 and 900 °C.

900 °C from 300 °C. Hence, nanoparticles synthesized at 300 and 900 °C are investigated using XANES-imaging.

XANES spectra extracted from these images from bulk mode (whole image) exhibit similar behavior with annealing temperature (Fig. S2†). In addition, main edge energy shift of Fe K-edge estimated from these measurements is 0.6 ± 2 eV (Fig. 8b) which appears to be similar (considering error values) to that determined from the XANES spectra shown in Fig. 8b.

As mentioned earlier, the XANES imaging measurements are able to give spatially resolved chemical information, hence, XANES spectrum are also extracted from single pixels by taking different pixels P_1, P_2 and P_3. Fe K-edge XANES spectra, extracted from P_1, P_2 and P_3 pixels of TXM images for $CoFe_2O_4$ nanoparticles synthesized at 300 and 900 °C are shown in Fig. 8. These measurements reveal that Fe K-edge XANES spectra remain almost similar in different regions of materials for lateral resolution down to 35 nm (Fig. 8a and b).

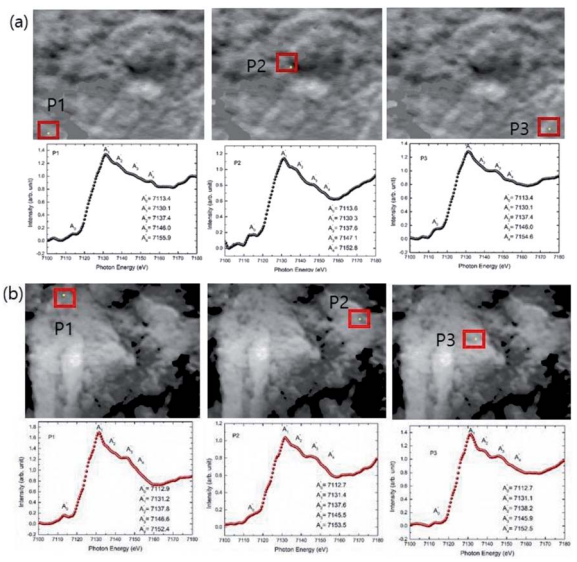

Fig. 8 The XANES spectra extracted on the 2-dimensional XANES-imaging results at Fe K-edge for $CoFe_2O_4$ nanoparticles synthesized at (a) 300 and (b) 900 °C for selected pixels P_1, P_2 and P_3.

Co L-edge spectra of these materials show spectral features B_1 and B_2 (Fig. 9a). These spectral features occur at 774.9 ± 0.1 and 778.0 ± 0.1 in the Co L-edge spectra of these nanoparticles. In addition, a shoulder around 776.1 ± 0.1 eV (shown by dotted arrow) is also observed in the spectra of all nanoparticles. Similar nature of Co L-edge spectra is reported for different kind of nanostructures of $CoFe_2O_4$.[52] Presence of these spectral features in Co L-edge spectra is associated with 2+ oxidation state in both tetrahedral and octahedral environment.[52] Co K-edge spectra show spectral features B_1', B_2' and B_3' centered at 7726.0 ± 0.4, 7733.7 ± 0.4 and 7741.8 ± 0.4 eV for all annealing temperatures (Fig. 9b). A minor pre-edge spectral feature, B_o', centered at 7708.9 ± 0.4 occurs in the spectra of these nanoparticles. Main edge occurs at 7716.6 ± 0.4, 7716.3 ± 0.4, 7716.2 ± 0.4 and 7716.1 ± 0.4 eV for nanoparticles synthesized at 300, 500, 700 and 900 °C. The main edge shifts towards lower value with annealing temperature in case of Co K-edge revealing the same oxidation state at all temperature. This main edge energy shift is 0.5 ± 0.8 eV when annealing temperature increases from 300 and 900 °C. These results are further supported by XANES-imaging spectra at Co K-edges for $CoFe_2O_4$ nanoparticles obtained at 300 and 900 °C. XANES (Fig. S3†). Moreover, Co K-edge spectra for different pixels P_1, P_2 and P_3 exhibit almost similar spectral features for each spectra of different nanoparticle system (Fig. 10a and b) revealing almost same local electronic structure of individual particles. These observations are concurrent with that obtained from Fe K-edge measurements.

Covalence and metal oxygen hybridization

To reveal the nature of metal oxygen hybridization in these nanoparticles, O K-edge NEXAFS measurements were performed and shown in Fig. 11. Pre-edge spectral features C_1 and C_2 appear at 529.1 ± 0.1 and 530.4 ± 0.1 eV at all annealing temperatures (Fig. 11a). Post-edge spectral features C_3, C_4, C_5 and C_6 centered at 536.9 ± 0.1, 540.2 ± 0.1, 546.8 ± 0.1 and 560.7 ± 0.1 eV appear in the O K-edge spectra of all

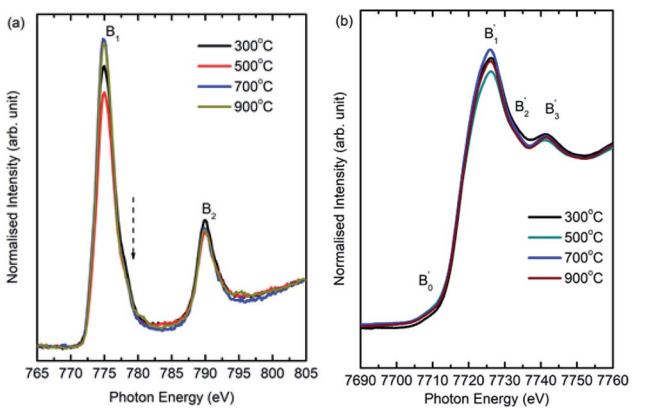

Fig. 9 (a) Co L-edge and (b) Co K-edge spectra of $CoFe_2O_4$ nanoparticles synthesized at 300, 500, 700 and 900 °C.

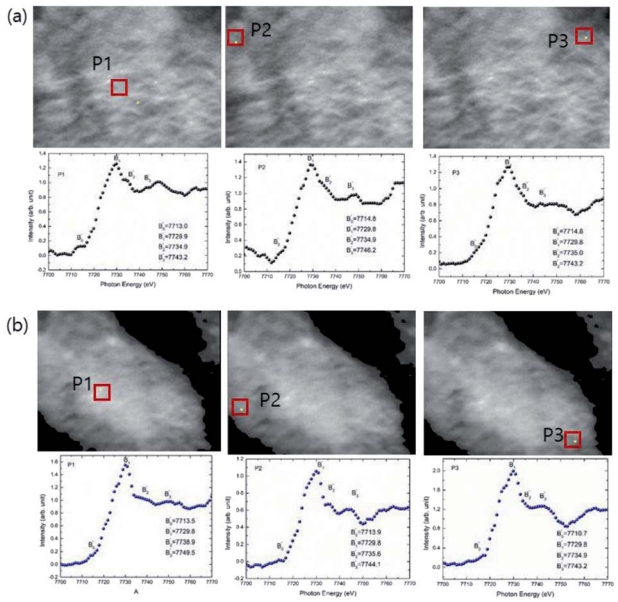

Fig. 10 The XANES spectra extracted on the 2-dimensional XANES-imaging results at Co K-edge for $CoFe_2O_4$ nanoparticles synthesized at (a) 300 and (b) 900 °C for selected pixels P_1, P_2 and P_3.

nanoparticles (Fig. 11a). Observed pre- and post-edge spectral features are characteristics of O K-edge spectrum of $CoFe_2O_4$ and reported in our previous studies as well as work from other groups.

Since, it is well established that pre-edge region of O K-edge spectrum reflect the extent of hybridization in ferrite/transition metal based nanoparticles,[8,53,54] hence, pre-edge region is critically analyzed. Spectral features C_1 and C_2 are associated with metal–oxygen hybridization in these nanoparticles and reflect the t_{2g} and e_g symmetry states. Thus, to determine the extent of hybridization in these nanoparticles, pre-edge region is deconvoluted into spectral features C_1 and C_2. The deconvoluted pre-edge regions for different annealing temperatures are shown in Fig. 11b. Ratio of t_{2g}/e_g was determined from these de-convoluted features to get quantitative information of metal–oxygen hybridization. t_{2g}/e_g ratio for these nanoparticles are 0.4, 0.6, 0.5 and 0.4 for annealing temperatures of 300, 500, 700 and 900 °C. Thus, these studies envisaged modulation of extent of hybridization with annealing temperature.[54,55]

Local atomic structure

To get insights of local atomic structure, EXAFS spectra at Co K and Fe K-edge are measured (Fig. S4†). These EXAFS spectra are simulated by considering the distribution of cations between A-site and B-site of spinel structure. Crystal information files (CIF) for these sites are generated based on positions of metal and oxygen ions in the unit cell of spinel structures using ATOMS (Table S2†).[12]

Co K-edge EXAFS investigations

The simulated chik spectra (Fig. S5†) and Fourier transform at Co K-edge for various annealing temperature are shown in Fig. 12a. Simulated parameters are collated in Table 2. Bond-distance for Co–O and Co–Co shells among A- and B-site along with fractions of metal ions (n_1 and n_2) are shown for various annealing temperatures. Co–O shell bond distances are 1.96 and 2.06 Å for A-site and B-site respectively. Co–Co shell bond distances are 3.48 and 2.94 Å for A-site and B-site respectively. Fractions of Co^{2+} ions attached to A-site (n_1) are 0.27 ± 0.05, 0.42 ± 0.06, 0.48 ± 0.03 and 0.34 ± 0.05 for annealing temperature of 300, 500, 700 and 900 °C. Fractions of these ions attached to B-site (n_2) are 0.58 ± 0.02, 0.51 ± 0.01, 0.65 ± 0.02 and 0.65 ± 0.04 for annealing temperature of 300, 500, 700 and 900 °C.

Fe K-edge EXAFS investigations

The simulated chik spectra (Fig. S6†) and Fourier transform at Fe K-edge are shown in Fig. 12b. Simulated parameters are collated in Table 3. Bond-distance for Fe–O and Fe–Fe shells among A- and B-site along-with fractions of Fe^{3+} ions (n_1 and n_2)

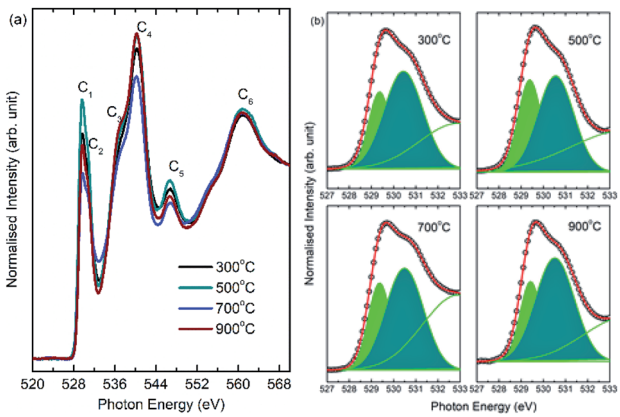

Fig. 11 (a) O K-edge spectra of $CoFe_2O_4$ nanoparticles annealed at 300, 500, 700 and 900 °C. (b) De-convoluted pre-edge region of O K-edge spectra at corresponding annealing temperature.

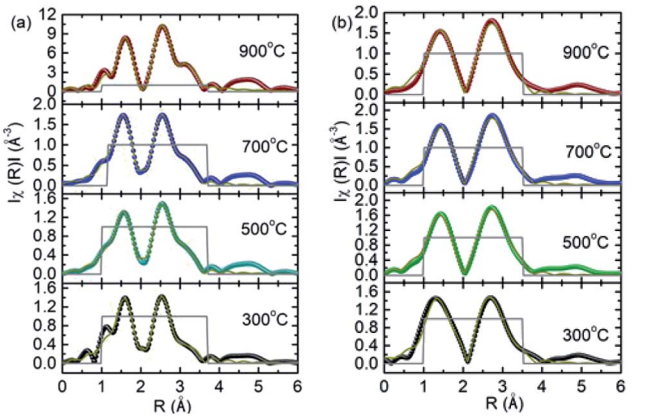

Fig. 12 Simulated non-phase corrected Fourier transform of (a) Co and (b) Fe K-edge EXAFS spectra for $CoFe_2O_4$ nanoparticles synthesized at 300, 500, 700 and 900 °C.

Table 2 Interatomic distance (R), co-ordination numbers (N), Debye–Waller factors (σ^2), and correction to energy (ε_o) of main edge obtained by fitting the experimental Fe–K edge EXAFS spectra. n_1 and n_2 are the fractions of co-ordination numbers (N) at A-site and B-sites

S.N.	Atoms	N	R (Å)	σ^2 (Å^2)	Atoms	N	R (Å)	σ^2 (Å^2)
300 °C; ε_o = 0.11 eV; *R*-factor: 0.002								
A-site ($n_1 = 0.27 \pm 0.05$)					B-site ($n_2 = 0.58 \pm 0.02$)			
1	O	4	1.96	0.004	O	6	2.06	0.004
2	Co	12	3.48	0.023	Co	6	2.94	0.005
3					Co	6	3.48	0.006
500 °C; ε_o = −0.039 eV; *R*-factor: 0.003								
A-site ($n_1 = 0.42 \pm 0.06$)					B-site ($n_2 = 0.51 \pm 0.02$)			
1	O	4	1.96	0.004	O	6	2.07	0.004
2	Co	12	3.46	0.012	Co	6	2.94	0.005
					Co	6	3.46	0.012
700 °C; ε_o = −0.78 eV; *R*-factor: 0.001								
A-site ($n_1 = 0.48 \pm 0.03$)					B-site ($n_2 = 0.65 \pm 0.02$)			
1	O	4	1.96	0.001	O	6	2.07	0.003
2	Co	12	3.47	0.011	Co	6	2.93	0.005
					Co	6	3.4	0.009
900 °C; ε_o = 0.14 eV; *R*-factor: 0.004								
A-site ($n_1 = 0.34 \pm 0.05$)					B-site ($n_1 = 0.65 \pm 0.04$)			
1	O	4	1.96	0.005	O	6	2.07	0.004
2	Co	12	3.47	0.010	Co	6	2.94	0.005
					Co	6	3.47	0.009

Table 3 Interatomic distance (R), co-ordination numbers (N), Debye–Waller factors (σ^2), and correction to energy (ε_o) of main edge obtained by fitting the experimental Fe–K edge EXAFS spectra

S.N.	Atoms	N	R (Å)	σ^2 (Å^2)	Atoms	N	R (Å)	σ^2 (Å^2)
300 °C; ε_o = −0.79 eV; *R*-factor: 0.01								
A-site ($n_1 = 0.33 \pm 0.08$)					B-site ($n_2 = 0.89 \pm 0.06$)			
1	O	4	1.82	−0.006	O	6	2.01	0.004
2	Fe	12	3.51	0.009	Fe	6	2.99	0.008
					Fe	6	3.50803	0.015
500 °C; ε_o = −2.32 eV; *R*-factor: 0.006								
A-site ($n_1 = 0.43 \pm 0.08$)					B-site ($n_2 = 0.83 \pm 0.05$)			
1	O	4	1.85	0.001	O	6	1.99	0.006
2	Fe	12	3.47	0.008	Fe	6	2.96	0.007
					Fe	6	3.47	0.008
700 °C; ε_o = −1.64 eV; *R*-factor: 0.006								
A-site ($n_1 = 0.40 \pm 0.05$)					B-site ($n_2 = 0.80 \pm 0.05$)			
1	O	4	1.84	0.003	O	6	1.98	0.006
2	Fe	12	3.48	0.006	Fe	6	2.96686	0.006
					Fe	6	3.48287	0.006
900 °C; ε_o = 4.1 ± 1.6 eV; *R*-factor: 0.01								
A-site ($n_1 = 0.5 \pm 0.2$)					B-site ($n_2 = 0.9 \pm 0.1$)			
1	O	4	1.82	0.003	O	6	1.98	0.004
2	Fe	12	3.47	0.009	Fe	6	2.97	0.008
					Fe	6	3.47	0.009

are shown for various annealing temperatures. Fe–O shell bond distances are 1.82 and 2.01.

Å for A- and B-site respectively. Fe–Fe shell bond distances are 3.51 and 2.98 Å for A-site and B-site respectively. Fractions of Fe^{3+} ions attached to A-site (n_1) are 0.33 ± 0.08, 0.43 ± 0.08, 0.40 ± 0.05 and 0.5 ± 0.2 for annealing temperature of 300, 500, 700 and 900 °C. Fractions of these ions attached to B-site (n_2) are 0.89 ± 0.06, 0.83 ± 0.05, 0.80 ± 0.05 and 0.9 ± 0.1 for annealing temperature of 300, 500, 700 and 900 °C.

Local magnetic structure

To understand the magnetic interaction in these nanoparticles, XMCD spectra for nanoparticles synthesized at 300 and 900 °C are shown in Fig. 13. XAS spectra under different helicity of X-ray exhibit spectral features S_1, A_1, S_2, A_3 and A_4 for these annealing temperatures (Fig. 13a and b: Upper panels). Origin of these spectral features are already discussed. Fig. 13a and b (Lower panels) also depicts MCD signal for these nanoparticles. Feature assigned as T is associated with presence of Fe^{3+} ions among tetrahedral sites, however, spectral features O_1 and O_2 is due to presence of these ions among octahedral sites.

Positive spectral features, T and negative spectral features O_1, O_2 in the MCD spectra of these nanoparticles are due to negative exchange interaction among Fe^{3+} ions situated at A- and B-sites.[56,57] Area of these spectral features is determined by de-convoluting these features (Fig. 13c). This envisages that almost 34% of Fe^{3+} ions reside on A-site, however, this fraction is almost 66% at A-site for nanoparticle synthesized at 300 °C. In

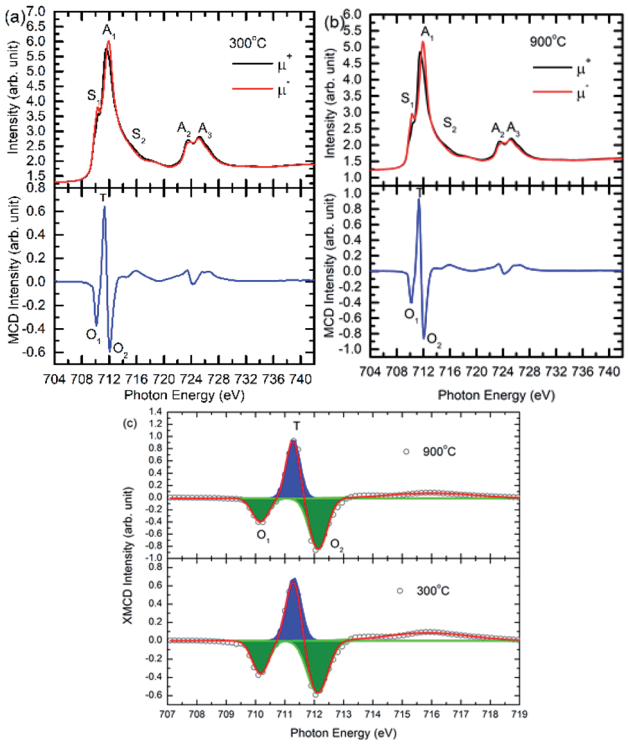

Fig. 13 XAS spectra (Upper panel) and MCD spectra (Lower Panel) of the $CoFe_2O_4$ nanoparticles synthesized at (a) 300 and (b) 900 °C. (c) De-convoluted L_3-edge of MCD signal for these nanoparticles. μ^+ and μ^- are the helicity of left and right circularly polarized light.

case of nanoparticles synthesized at 900 °C, these fractions are 31% and 69% for A- and B-sites respectively.

Discussion

Thus, EXAFS and XMCD investigations envisage redistribution of cations with annealing temperature/crystallite size. To determine exact occupancy of metal ions from EXAFS following relation was used.

For Co^{2+} ions,

$$\frac{1-\lambda}{\lambda} = \frac{n_2}{n_1} \tag{11}$$

For Fe^{3+} ions,

$$\frac{1+\lambda}{1-\lambda} = \frac{n_2}{n_1} \tag{12}$$

Values of λ are estimated from these relations that are used to determine occupancies of Co^{2+} and Fe^{3+} ions (Table 4). Occupancies determined from EXAFS are similar to that obtained from XRD (Tables 1 and 4).

The theoretical magnetic moment of ferrite is given as

$$m = m_{\text{B-site}} - m_{\text{A-site}} \tag{13}$$

Based on structural formula mention in eqn (1), the magnetic moment of ferrite can be derived directly from magnetic moments of it's constituent Co^{2+} and Fe^{3+} ions from the equation given below

$$m = \left(m_{1-\lambda}^{Co^{2+}} + m_{1+\lambda}^{Fe^{3+}}\right)_{\text{B-site}} - \left(m_{\lambda}^{Co^{2+}} + m_{1-\lambda}^{Fe^{3+}}\right)_{\text{A-site}} \tag{14}$$

The magnetic moment of each nanoparticles was determined using eqn (14) by taking magnetic moment of Fe^{3+} and Co^{2+} ions as 5.92 and 3.87 μ_B.[58] The magnetic moments estimated from these relation are 5.3, 5.0, 4.5 and 4.5 μ_B for nanoparticles synthesized at 300, 500, 700 and 900 °C (Table 4).

Table 4 Distribution of metal ions determined from EXAFS and calculation of effective magnetic moment in Bohr magneton (μ_B)

			$CoFe_2O_4$ nanoparticles			
Parameters			300 °C	500 °C	700 °C	900 °C
Occupancy	A-site	Co^{2+}	0.31	0.45	0.42	0.35
		Fe^{3+}	0.54	0.60	0.67	0.71
	B-site	Co^{2+}	0.49	0.55	0.58	0.65
		Fe^{3+}	1.46	1.40	1.33	1.29
Magnetic moment		A-site	5.2	5.3	5.6	5.6
		B-site	10.5	10.4	10.1	10.1
Effective magnetic moment (μ_B)			5.3	5.0	4.5	4.5
Experimental magnetic moment (μ_B)			2.2	2.8	2.9	3.4

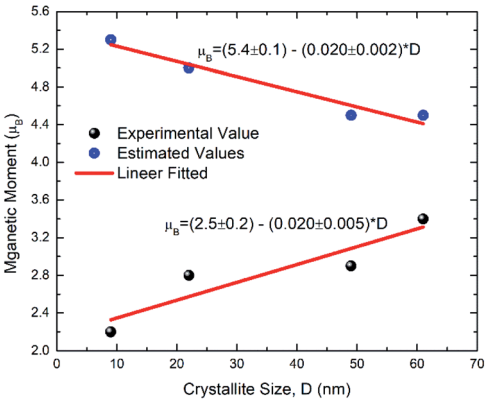

Fig. 14 Experimental and estimated values of magnetic moment.

The experimentally observed value of magnetic moment for these nanoparticles are 2.2, 2.8, 2.9 and 3.4 μ_B (Table 4). Thus, difference among the theoretical and experimentally observed values of magnetic moment is large for lower crystallite size nanoparticles (Fig. 14). The other factors which affect the magnetization are spin canting[59] and formation of spin-glass state at the surface.[60,61] These factors diminishes the magnetization in ferrite nanoparticles.[59–62] Hence, the spin canting and spin-glass state effects rather than particle size effects or cation redistribution influences the magnetic behavior of these nanoparticles.

Conclusions

In conclusion, pure cubic spinel phase of synthesized $CoFe_2O_4$ nanoparticles was observed. Both the crystallite/particle size increases with annealing temperature. The particle shape also modifies from spherical to hexagonal type with increase of annealing. All nanoparticles exhibit ferrimagnetic behavior with linear increase of saturation magnetization and magnetic moment with enhancement of crystallite size. Variation of other magnetic parameters like remanent magnetization and coercivity reflects the single domain behavior below 55 nm. Moreover, optical band-gap of these nanoparticle is influenced by optical confinement.

The nanoparticles exhibit modification of Co, Fe (3d)–O (2p) hybridized states with increase of annealing temperature as envisaged from the O K-edge NEXAFS spectra. The presence of Fe and Co ions in 3+ and 2+ state is evidenced from the Fe and Co L-edge NEXAFS, XANES and spatially resolved XANES-imaging techniques. Distribution of Fe and Co ions estimated from EXAFS simulation corroborates the results obtained from Rietveld refinement of X-ray diffraction patterns. XMCD revealed the negative exchange interaction among the metal ions situated at A- and B-sites.

Author's contribution

JPS conceptualised the work, performed analysis and wrote the manuscript in consultation with SL and KHC. JPS, JYP and SL

performed the XANES-imaging experiment and analysed the results. SHK, WCL performed the SEM, UV-Vis and XRD measurements. JPS, HK measured and analysed the hysteresis curves. VS and KHC performed the XAS experiments and simulated the obtained results. JPS, YHK and KHC carried out the XMCD measurements.

Conflicts of interest

Authors declare no conflicts of interests.

Acknowledgements

The research program of Commercializations Promotion Agency for R&D Outcomes (COMPA) funded by the Ministry of Science and ICT (1711080502), financially supports this research. KHC acknowledges the financial support received by Korea Institute of Science and Technology, Seoul, Republic of Korea through project no. 2V08170.

Notes and references

1 X. Cai, K. Chen, X. Gao, C. Xu, M. Sun, G. Liu, X. Guo, Y. Cai, B. Huang, J. Deng, J. Z. Liu, A. Tricoli, N. Wang, C. Dwyer and Y. Zhu, *Chem. Mater.*, 2019, **31**, 5769.
2 T. Bernges, J. Peilstöcker, M. Dutta, S. Ohno, S. P. Culver and K. Biswas, *Inorg. Chem.*, 2019, **58**, 9236.
3 C. V. Ovidiu Garlea, V. Yannello, H. Cao and A. F. Bangura, *Inorganic Chemistry*, 2019, **58**(9), 5799.
4 C. Richard and A. Catlow, *Philos. Trans. R. Soc., A*, 2015, **373**, 20130162.
5 X. Liu and T.-C. Weng, *MRS Bull.*, 2016, **41**, 466.
6 G. van der Laan and A. I. Figueroa, *Coord. Chem. Rev.*, 2014, **95**, 129.
7 A. Sakdinawat and D. Attwood, *Nat. Photonics*, 2010, **4**, 840.
8 J. P. Singh, S. H. Kim, S. O. Won, W. C. Lim, I. Lee and K. Hwa Chae, *CrystEngComm*, 2016, **18**, 2701.
9 K. Kumari, R. Naji Aljawfi, Y. S. Katharria, S. Dwivedi, K. H. Chae, R. Kumar, A. Alshoaibi, P. A. Alvi, S. Dalela and S. Kumar, *J. Electron Spectrosc. Relat. Phenom.*, 2019, **235**, 29.
10 S. Jauhar, J. Kaur, A. Goyal and S. Singhal, *RSC Adv.*, 2016, **6**, 97694.
11 A. Varma, A. S. Mukasya, A. S. Rogachev and K. V. Manukyan, *Chem. Rev.*, 2016, **116**, 14493–14586.
12 E. Lottini, A. López-Ortega, G. Bertoni, S. Turner, M. Meledina, G. Van Tendeloo, C. de Julián Fernández and C. Sangregorio, *Chem. Mater.*, 2016, **28**, 4214.
13 A. V. Ramosa, M.-J. Guittet, J.-B. Moussy, R. Mattana, C. Deranlot, F. Petroff and C. Gatel, *Appl. Phys. Lett.*, 2007, **91**, 122107.
14 D. Moitra, M. Chandel, B. Kumar Ghosh, R. Kumar Jani, M. Kumar Patra, S. Raj Vadera and N. N. Ghosh, *RSC Adv.*, 2016, **6**, 76759.
15 N. Xu, J. Qiao, Q. Nie, M. Wang, He Xu, Y. Wang and X. Zhou, *Catal. Today*, 2018, **315**, 144.
16 S. Permien, S. Indris, U. Schürmann, L. Kienle, S. Zander, S. Doyle and W. Bensch, *Chem. Mater.*, 2016, **28**, 434.
17 S. Y. Srinivasan, K. M. Paknikar, D. Bodas and V. Gajbhiye, *Nanomedicine*, 2018, **13**, 1221.
18 B. D. Cullity, *Introduction to Magnetic Mater*, 1972.
19 H. Kumar, R. C. Srivastava, J. P. Singh, P. Negi, H. M. Agrawal, D. Das and K. Hwa Chae, *J. Magn. Magn. Mater.*, 2016, **401**, 16.
20 M. Artus, L. Ben Tahar, F. Herbst, L. Smiri, F. Villain, N. Yaacoub, J. Grenèche, S. Ammar and F. Fiévet, *J. Phys.: Condens. Matter*, 2011, **23**, 506001.
21 H. Kumar, J. P. Singh, R. Chandra Srivastava, P. Negi, H. M. Agrawal, K. Asokan, S. Ok Won and K. Hwa Chae, *J. Alloys Compd.*, 2015, **645**, 274.
22 D. Sharma and N. Khare, *AIP Adv.*, 2016, **6**, 085005.
23 C. Singh, A. Goyal and S. Singhal, *Nanoscale*, 2014, **6**, 7959.
24 J. P. Singh, G. Dixit, R. C. Srivastava, H. M. Agrawal, V. R. Reddy and A. Gupta, *J. Magn. Magn. Mater.*, 2012, **324**, 2553.
25 M. Tsvetkov, M. Milanova, I. Ivanova, D. Neov, Z. Cherkezova-Zheleva, J. Zaharieva and M. Abrashev, *J. Mol. Struct.*, 2019, **1179**, 233.
26 J. P. Singh, S. Ok Won, W. Cheol Lim, I. Jae Lee and K. H. Chae, *J. Mol. Struct.*, 2016, **1108**, 444.
27 J. P. Singh, B. Kaur, A. Sharma, S. Hee Kim, S. Gautam, R. C. Srivastava, N. Goyal, W. Cheol Lim, H.-J. Lin, J. M. Chen, K. Asokan, D. Kanjilal, S. O. Won, I.-J. Lee and K. H. Chae, *Phys. Chem. Chem. Phys.*, 2018, **20**, 12084.
28 H. Kumar, J. P. Singh, R. C. Srivastava, K. R. Patel and K. Hwa Chae, *Superlattices Microstruct.*, 2017, **109**, 296.
29 J. P. Singh, S. Lee and K. H. Chae, *Vacuum*, 2019, **168**, 108848.
30 H. Hwi Lee, M. Kumar and H. Joon Shin, *Physics and Advanced Technology*, 2017, **26**, 7.
31 H. J. Lee, G. Kim, D. H. Kim, J.-S. Kang, C. L. Zhang, S.-W. Cheong, J. H. Shim, S. Lee, H. Lee and J.-Y. Kim, *J. Phys.: Condens. Matter*, 2008, **20**, 295203.
32 S. Lee, I. H. Kwon, J.-Y. Kim, S. S. Yang, S. Kang and J. Lim, *J. Synchrotron Radiat.*, 2017, **24**, 1276.
33 J. Y. Park, J. P. Singh, J. Lim, K. H. Chae and S. Lee, *Mater. Lett.*, 2020, **261**, 126983.
34 B. Ravel and M. Newville, *J. Synchrotron Radiat.*, 2005, **12**, 537.
35 A. L. Ankudinov, B. Ravel, J. J. Rehr and S. D. Conradson, *Phys. Rev. B: Condens. Matter Mater. Phys.*, 1998, **58**, 7565.
36 J. Y. Park, J. P. Singh, J. Lim and S. Lee, *J. Synchrotron Radiat.*, 2020, **27**, 545.
37 T. Meron, Y. Rosenberg, Y. Lereah and G. Markovich, *J. Magn. Magn. Mater.*, 2005, **292**, 11.
38 J. P. Singh, R. C. Srivastava, H. M. Agrawal and P. Chand, *Int. J. Nanosci.*, 2009, **8**, 523.
39 G. A. Kaur, M. Shandilya, P. Rana, S. Thakur and P. Uniyal, *Nano-Structures & Nano-Objects*, 2020, **22**, 100428.
40 D. M. Ghone, V. L. Mathe, K. K. Patankar and S. D. Kaushik, *J. Alloys Compd.*, 2018, **739**, 52.
41 A. S. Ponce, E. F. Chagas, R. J. Prado, C. H. M. Fernades, A. J. Terezo and E. B. Saitovitch, *J. Magn. Magn. Mater.*, 2013, **344**, 182.
42 A. López-Ortega, E. Lottini, C. de Julián Fernández and C. Sangregorio, *Chem. Mater.*, 2015, **27**, 4048.

43 J. P. Singh, G. Dixit, R. C. Srivastava, H. M. Agrawal and R. Kumar, *J. Alloys Compd.*, 2013, **551**, 370.
44 R. S. Yadav, I. Kuřitka, J. Vilcakova, J. Havlica, J. Masilko, L. Kalina, J. Tkacz, J. Švec, V. Enev and M. Hajdúchová, *Adv. Nat. Sci.: Nanosci. Nanotechnol.*, 2017, **8**, 045002.
45 Z. Ž. Lazarević, Č. Jovalekić, D. Sekulić, M. Slankamenac, M. Romceevic, A. Milutinović and N. Ž. Romčević, *Sci. Sintering*, 2012, **44**, 331.
46 R. Zhang, Q. Yuan, R. Ma, X. Liu, C. Gao, M. Liu, C.-L. Jia and H. Wang, *RSC Adv.*, 2017, **7**, 21926.
47 Q. Li, C. W. Kartikowati, S. Horie, T. Ogi, T. Iwaki and K. Okuyama, *Sci. Rep.*, 2017, **7**, 9894.
48 J. Llanos, C. Mujica and A. Buljan, *J. Alloys Compd.*, 2001, **316**, 146–152.
49 J. P. Singh, R. C. Srivastava and H. M. Agrawal, *AIP Conf. Proc.*, 2010, **1276**, 137.
50 S. T. Tan, B. J. Chen, X. W. Sun, W. J. Fan, H. S. Kowk, X. H. Xhang and S. J. Chua, *J. Appl. Physiol.*, 2005, **98**, 013505.
51 B. Gilbert, J. E. Katz, J. D. Denlinger, Y. Yin, R. Falcone and G. A. Waychunas, *J. Phys. Chem. C*, 2010, **114**, 21994.
52 S. Nappini, E. Magnano, F. Bondino, P. Igor, A. Barla, E. Fantechi, F. Pineider, C. Sangregorio, L. Vaccari, L. Venturelli and P. Baglioni, *J. Phys. Chem. C*, 2015, **119**, 25529.
53 J. P. Singh, J. Y. Park, K. H. Chae, D. Ahn and S. Lee, *Nanomaterials*, 2020, **10**, 759.
54 S. Shen, J. Zhou, C.-L. Dong, Y. Hu, E. Nestor Tseng, P. Guo, L. Guo and S. S. Mao, *Sci. Rep.*, 2014, **4**, 6627.
55 J. P. Singh, H. Kuang, S. Lee and K. H. Chae, Investigation of Metal–Oxygen Hybridization Process during the Growth of ZnFe2O4 Films on MgO (100) Substrates, (to be communicated).
56 P. M. Zélis, G. A. Pasquevich, K. L. S. Rodríguez, F. H. Sánchez and C. E. Rodríguez Torres, *J. Magn. Magn. Mater.*, 2016, **419**, 98.
57 C. E. R. Torres, G. A. Pasquevich, P. Mendoza Zélis, F. Golmar, S. P. Heluani, S. K. Nayak, W. A. Adeagbo, W. Hergert, M. Hoffmann, A. Ernst, P. Esquinazi and S. J. Stewart, *Phys. Rev. B: Condens. Matter Mater. Phys.*, 2014, **89**, 104411.
58 K. C. de Berg and K. J. Chapman, *J. Chem. Educ.*, 2001, **78**, 670.
59 T. J. Daou, J. M. Greneche, S. J. Lee, S. Lee, C. Lefevre, S. Bégin-Colin and G. Pourroy, *J. Phys. Chem. C*, 2010, **114**, 8794.
60 F. Zeb, W. Sarwer, K. Nadeem, M. Kamran, M. Mumtaz, H. Krenn and I. Letofsky-Papst, *J. Magn. Magn. Mater.*, 2016, **407**, 241.
61 J. Mantilla, L. León Félix, M. A. R. Martinez, P. Souza, P. A. M. Rodrigues, L. C. Figueiredo, S. W. da Silva, J. A. H. Coaquira, F. F. H. Aragón and P. C. Morais, *J. Magn. Magn. Mater.*, 2019, **476**, 392.
62 J. P. Singh, R. C. Srivastava, H. M. Agrawal, R. Kumar, V. R. Reddy and A. Gupta, *J. Magn. Magn. Mater.*, 2010, **322**, 1701.